








RESEARCH ARTICLE | APRIL 13 2023

Macroscopic shaping of coordination polymer via crystal–glass phase transformation as monolithic catalyst for efficient catalyst recovery ^F

Special Collection: [Challenges and Perspectives in Materials Chemistry—A Celebration of Prof. Sir Anthony K. Cheetham's 75th Birthday](#)

Thanakorn Tiyawarakul ; Thidarat Imyen  ; Kanokwan Kongpatpanich ; Teerat Watcharatpong ; Satoshi Horike  



APL Mater 11, 041119 (2023)

<https://doi.org/10.1063/5.0144603>



CrossMark

AMERICAN ELEMENTS
THE ADVANCED MATERIALS MANUFACTURER®

Li	Be	B	C	N	O	F	Ne										
Na	Mg	Al	Si	P	S	Cl	Ar										
K	Ca	Sc	Ti	V	Cr	Mn	Fe	Co	Ni	Cu	Zn	Ga	Ge	As	Se	Br	Kr
Rb	Sr	Y	Zr	Nb	Mo	Tc	Ru	Rh	Pd	Ag	Cd	In	Sn	Sb	Te	I	Xe
Cs	Ba	La	Hf	Ta	W	Re	Os	Ir	Pt	Au	Hg	Tl	Pb	Bi	Po	At	Rn
Fr	Ra	Ac	Rf	Db	Sg	Bh	Hs	Mt	Ds	Rg	Cn	Nh	Fl	Mc	Lv	Ts	Og
		Ce	Pr	Nd	Pm	Sm	Eu	Gd	Tb	Dy	Ho	Er	Tm	Yb	Lu		
		Th	Pa	U	Np	Pu	Am	Cm	Bk	Cf	Es	Fm	Md	No	Lr		

Now Invent.™

www.americanelements.com

yttrium iron garnet glassy carbon beamsplitters fused quartz additive manufacturing

zeolites III–IV semiconductors gallium lump copper nanoparticles organometallics

nano ribbons barium fluoride europium phosphors photonics infrared dyes

sapphire windows Nd:YAG epitaxial crystal growth ultra high purity materials transparent ceramics CIGS

spintronics raman substrates cerium oxide polishing powder cermet nanodispersions

silver nanoparticles perovskites surface functionalized nanoparticles MBE grade materials thin film

MOCVD beta-barium borate OLED lighting solar energy

rare earth metals quantum dots sputtering targets fiber optics

osmium scintillation Ce:YAG h-BN deposition slugs

refractory metals laser crystals CVD precursors photovoltaics

anodic aluminum oxide niobate InAs wafers metamaterials borosilicate glass

ZnS CdTe MOFs AuNPs YBCO superconductors InGaAs

perovskite crystals transparent ceramics indium tin oxide MgF₂ rutile optical glass

diamond micropowder

The Next Generation of Material Science Catalogs

© 2001–2022, American Elements LLC, a U.S. Registered Trademark

Macroscopic shaping of coordination polymer via crystal–glass phase transformation as monolithic catalyst for efficient catalyst recovery

Cite as: APL Mater. 11, 041119 (2023); doi: 10.1063/5.0144603

Submitted: 31 January 2023 • Accepted: 28 March 2023 •

Published Online: 13 April 2023




View Online



Export Citation



CrossMark

Thanakorn Tiyawarakul,¹  Thidarat Imyen,^{2a)}  Kanokwan Kongpatpanich,¹  Teerat Watcharatpong,¹ 
and Satoshi Horike^{1,2,3a)} 

AFFILIATIONS

¹ Department of Materials Science and Engineering, School of Molecular Science and Engineering, Vidyasirimedhi Institute of Science and Technology (VISTEC), Rayong 21210, Thailand

² Institute for Integrated Cell-Material Sciences, Institute for Advanced Study, Kyoto University, Yoshida-Honmachi, Sakyo-ku, Kyoto 606-8501, Japan

³ Department of Synthetic Chemistry and Biological Chemistry, Graduate School of Engineering, Kyoto University, Katsura, Nishikyo-ku, Kyoto 615-8510, Japan

Note: This paper is part of the Special Topic on Challenges and Perspectives in Materials Chemistry—A Celebration of Prof. Sir Anthony K. Cheetham's 75th Birthday.

^{a)} **Authors to whom correspondence should be addressed:** imyen.thidarat.7f@kyoto-u.ac.jp and horike@icems.kyoto-u.ac.jp

ABSTRACT

To circumvent the difficult processability and recovery of catalytic materials in powder form, we herein report macroscopic shaping of 1D coordination polymer consisting of zinc ions, orthophosphate, and benzimidazole, namely ZnPBIm, motivated by the crystal–glass phase transformation. Glassy ZnPBIm monoliths with different shapes and sizes were prepared via a melt–quench process without using the secondary component. As a heterogeneous acid catalyst, the glassy ZnPBIm monoliths contribute to the esterification of levulinic acid with ethanol at 100 °C with recyclability for at least three consecutive cycles, and over 90% of catalyst mass was recovered. The macroscopic shape of the monoliths was retained after 24 h of reaction. Surface crystallization of glassy ZnPBIm was induced by the presence of water during esterification, and the glass domain serves as a macroscopic support for the crystallized domain.

© 2023 Author(s). All article content, except where otherwise noted, is licensed under a Creative Commons Attribution (CC BY) license (<http://creativecommons.org/licenses/by/4.0/>). <https://doi.org/10.1063/5.0144603>

I. INTRODUCTION

Shaping of heterogeneous catalytic materials at the macroscopic scale with controllable shapes realizes the catalyst utilization efficiency toward the practical applications in terms of convenient handling, recovery, and recyclability, especially for liquid-phase catalysis. In addition, the macroscopic structures can prevent the compaction of the catalyst by fluid flow in a fixed-bed reactor and a pressure drop across the column can be subsequently reduced.¹ Up until now, many efforts have been made to form bulk architectures of coordination polymer (CP)/metal–organic framework (MOF)

catalysts by using monolithic supports, blending in polymeric substrates, and mechanical pressing with or without binders.^{2–4} The effective loadings in these substrates are limited. The presence of binders reduces the accessibility of the active components to the guest molecules due to the coverage of the binder on the surfaces of CP/MOFs.⁵ In order to obtain pure CP/MOF bulk materials, the shaping approaches without using the secondary component are highly sought after.

In the past several years, the crystal melting and the subsequent glass formation via quenching of CP/MOFs have gained research interest and the library of melting CP/MOFs has been expanded.^{6–12}

The resultant CP/MOF glasses with non-crystalline nature and preserved short-range order have demonstrated various properties with respect to their crystalline counterparts, for example, optical transparency, mechanical stability and flexibility, and ionic/electronic conductivities.^{11–15} Upon heating meltable CP/MOFs above their melting temperature (T_m), the liquid state provides flowability and moldability. In view of macroscopic shaping without using monolithic supports and binders, these melting CP/MOFs can be potentially shaped in different sizes and forms via the melt-quenching approach. Despite this inherent advantage of the moldable character, the meltable CP/MOFs have not been pursued as shapable monolithic catalysts.

In this work, meltable CP $[\text{Zn}_3(\text{H}_2\text{PO}_4)_6(\text{H}_2\text{O})_3](\text{Hblm})$ (ZnPBlm; Hblm:1,3-benzimidazole) was chosen as an example to realize macroscopic shaping of heterogeneous catalyst via the crystal–glass phase transformation.¹⁶ Motivated by the active protons in the structure, ZnPBlm was utilized in acid-catalyzed reaction, namely esterification of levulinic acid (LA) with ethanol to produce ethyl levulinate (EL). EL is an important compound in the flavoring and fragrance industries as well as biofuel modification.¹⁷ A typical esterification process for EL production is carried out in a liquid phase and catalyzed by mineral acids, such as H_3PO_4 , H_2SO_4 , and HCl, all of which are corrosive and unrecyclable. ZnPBlm was shaped with different macroscopic shapes and sizes using melt-molding technique followed by the quenching process. We then evaluated their catalytic performances depending on the shapes.

II. EXPERIMENTAL

A. Synthesis and glass formation of $[\text{Zn}_3(\text{H}_2\text{PO}_4)_6(\text{H}_2\text{O})_3](\text{Hblm})$ (ZnPBlm)

All chemicals were of reagent grade and used without further purification. ZnPBlm was synthesized by mechanochemistry following the previous work with some modifications.⁷ In a typical synthesis, 0.15 mmol of zinc oxide (Sigma-Aldrich), 5 mmol of benzimidazole (98%, TCI), and 30 mmol of phosphoric acid (85% in H_2O , TCI) were put in a 25-ml Teflon jar with a 15-mm steel-core Teflon ball. After the jar was shaken at 25 Hz for 60 min in a Retch MM400 grinder mill, the obtained white powder was washed with methanol. Then, ZnPBlm product was evacuated at room temperature overnight.

A glassy ZnPBlm monolith denoted as ZnPBlm-g was prepared by melting 0.15 g of crystalline ZnPBlm at 175 °C and quenching to room temperature in a glass vessel under an inert atmosphere. To shape ZnPBlm-g into different shapes and sizes, the melted ZnPBlm was transferred into a silicone mold at 120 °C and quenched to –35 °C for 5 min.

B. Material characterization

Powder x-ray diffraction (PXRD) patterns were collected using a Rigaku SmartLab SE x-ray type $\text{CuK}\alpha$ ($\lambda = 1.54059 \text{ \AA}$). Thermogravimetric analysis (TGA) and differential thermal analysis (DTA) were performed using a Rigaku Thermo plus TG 8122 under a N_2 flow of 200 ml min^{-1} from room temperature to 500 °C with a heating rate of $10^\circ \text{C min}^{-1}$. Differential scanning calorimetry (DSC) was measured using a 20 Perkin Elmer model-lab system-8500 under a N_2 flow of 20 ml min^{-1} . Fourier transform infrared (FTIR) spectra

were recorded using a Bruker ALPHA II FT-IR spectrometer with a Universal ATR accessory under N_2 atmosphere at room temperature. Scanning electron microscope (SEM) images were taken on a JEOL JSM-7610F operated with an acceleration voltage of 200 kV. Prior to each SEM analysis, the samples were sputtered with Pt at 10 mA for 120 s. ^1H and ^{31}P nuclear magnetic resonance (NMR) were carried out using a Bruker Avance III HD 600 MHz. The catalyst samples were digested in 1M HCl and dissolved in D_2O for NMR measurement. For NMR measurement of the reaction mixture, the experiment was carried out in $\text{DMSO-}d_6$. CHN elemental analysis was performed using a LECO TruSpec Micro Element Series with cystine standard. Inductively coupled plasma-optical emission spectrometry (ICP-OES) for quantitative analysis of Zn and P amounts was conducted using an Agilent 700 series. Before the ICP-OES experiment, the samples were digested in 2% HNO_3 with the total volume of 10 ml. Dynamic mechanical analysis (DMA) was performed under a N_2 flow with 0.05% strain using a Discovery Hybrid Rheometer HR20-TA instrument with an 8 mm rotational parallel-plate rheometer.

C. Catalytic performance testing for esterification of levulinic acid (LA) with ethanol to ethyl levulinate (EL)

Esterification of LA with ethanol was carried out in a tightly closed cylindrical pressure glass vessel using 0.15 g of the catalyst and an equimolar mixture of LA (1.0 ml) and ethanol (0.59 ml) in toluene solvent (5 ml) under stirring at 250 rpm. The esterification reaction was conducted at 100 °C and autogenous pressure for 24 h. In a typical batch process, the reaction mixture was sampled at the initial (0 h) and final states (24 h). Gas chromatograph (PerkinElmer Clarus 680) equipped with a FID detector and an elite-wax capillary column was used to analyze the collected reaction mixture by using $67 \mu\text{l}$ of decane as an internal standard. LA conversion and EL selectivity were calculated by Eqs. (1) and (2), respectively,

$$\text{LA conversion (\%)} = \frac{\text{mole LA}_{\text{initial}} - \text{mole LA}_{\text{final}}}{\text{mole LA}_{\text{initial}}} \times 100, \quad (1)$$

$$\text{EL selectivity (\%)} = \frac{\text{mole EL formed}}{\text{mole all products formed}} \times 100. \quad (2)$$

III. RESULTS AND DISCUSSION

A. Structural characterization and glass formation of ZnPBlm

As reported in the literature,⁷ the crystal structure of ZnPBlm is composed of 1D chains of three octahedral Zn^{2+} ions bridged with six phosphates $[\text{Zn}_3(\text{H}_2\text{PO}_4)_6 \text{ units}]$ and coordinated with water molecules [Fig. 1(a)]. Each phosphate consists of two protons, which exhibit Brønsted acidity. Benzimidazole molecules locate between 1D chains stacking in a manner that they are surrounded by six chains. The powder x-ray diffraction (PXRD) pattern of the synthesized ZnPBlm matches with the simulated pattern obtained from the crystal structure [Figs. 1(b-i) and 1(b-ii)].

ZnPBlm exhibits thermal dehydration at 72 °C, crystal melting at 164 °C, and glass transition at 40 °C [Figs. 1(c) and S1] without crystallization or decomposition upon further heating up to 180 °C. A process of melting ZnPBlm at 175 °C and subsequently quenching

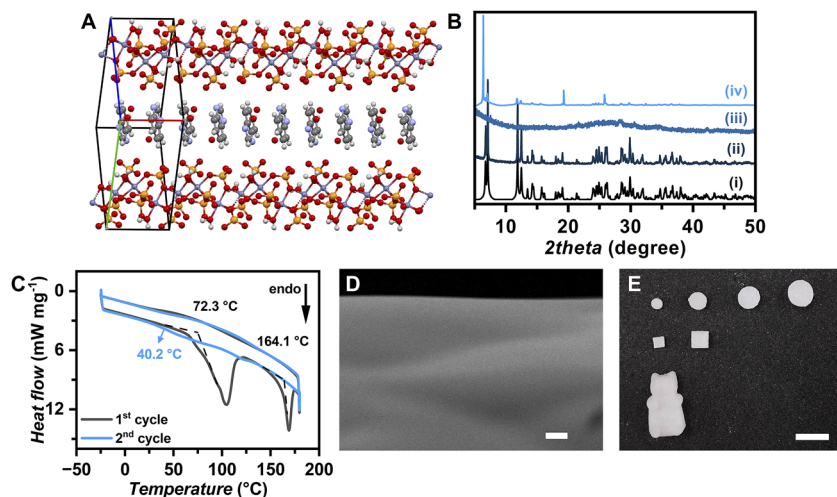


FIG. 1. (a) Crystal structure of ZnPBIm. The Zn, P, O, N, C, and H atoms are shown in purple, yellow, red, blue, gray, and white color, respectively. (b) PXRD patterns of (i) the simulated pattern of ZnPBIm from the single crystal x-ray structure, (ii) ZnPBIm, (iii) ZnPBIm-g, and (iv) ZnPBIm-g after LA esterification for 24 h. (c) DSC profile of ZnPBIm. The first and second cycles are shown in black and blue, respectively. (d) SEM image of ZnPBIm-g. ZnPBIm-g is the gray part, and carbon tape is the black part (the scale bar is 1 μm). (e) Photograph of ZnPBIm-g monoliths with various shapes and sizes (the scale bar is 10 mm).

it to room temperature under N_2 atmosphere yields glassy ZnPBIm denoted as ZnPBIm-g without the crystalline phase remained as confirmed by the PXRD [Fig. 1(b-iii)]. The dynamic mechanical analysis (DMA) performed in the frequency sweep mode confirms the glass transition of ZnPBIm-g by the change of mechanical properties above its T_g (Fig. S2). At 30 $^\circ\text{C}$ (below T_g), the storage modulus of ZnPBIm-g is higher than the loss modulus. This observation corresponds to a solid-like behavior. By increasing the temperature to 100 $^\circ\text{C}$ (above T_g), the loss modulus of ZnPBIm-g becomes higher than the storage modulus. This indicates that ZnPBIm-g softens above T_g , confirming its glassy behavior.

SEM images reveal the morphology change of ZnPBIm from polycrystalline grains with average crystal size of $\sim 1.3 \mu\text{m}$ of crystalline ZnPBIm (Fig. S3) to smooth surfaces without grain boundaries of ZnPBIm-g [Fig. 1(d)] after melt-quenching. Fourier transform infrared (FTIR) spectra of both crystalline ZnPBIm and ZnPBIm-g samples show a N–H stretching feature of benzimidazole at 2500–3200 cm^{-1} , indicating that benzimidazole is retained in ZnPBIm-g after the melt-quench process (Fig. S4). As determined by the CHN elemental analysis and inductively coupled plasma (ICP) (Tables SI and SII), the identical compositions of pristine ZnPBIm and ZnPBIm-g confirm that ZnPBIm-g undergoes crystal–glass phase transformation without the decomposition and chemical reaction.¹⁸

To demonstrate the processability of ZnPBIm into various shapes and sizes, we performed the shape engineering of ZnPBIm at macroscopic level based on its flowability during crystal melting. By using different silicone molds in the melt-molding process, ZnPBIm-g monoliths with regular and irregular shapes were obtained [Fig. 1(e)].

B. Catalytic performance of shaped ZnPBIm-g in esterification of levulinic acid with ethanol

To demonstrate the benefit in terms of catalyst recovery of macroscopic ZnPBIm-g monoliths prepared via crystal–glass phase transformation, they were employed as acid catalysts in esterification of levulinic acid (LA) with ethanol to ethyl levulinate (EL). The

reaction scheme is shown in Fig. 2(a). The catalytic performance is expressed in terms of LA conversion (%) and EL selectivity (%). Crystalline ZnPBIm was melt-quenched to form ZnPBIm-g in the reaction vessel [Fig. S5(a)]. As shown in Fig. 2(b), LA conversion over ZnPBIm-g increased with increasing reaction time. We carried out a blank experiment in the absence of catalyst and obtained LA conversion of 23% after 24 h of reaction (Table 1). In general, the reaction of LA with primary alcohols, such as ethanol, is auto-catalyzed due to the acidity of LA, but the reaction rate is low.¹⁹ ZnPBIm-g catalyzes LA esterification with respect to the blank experiment under the present condition. EL selectivity of 100% is achieved in all cases. For the catalytic recycling test, LA conversion on ZnPBIm-g is comparable through the total of three consecutive cycles [Fig. 2(c)]. Each catalytic cycle shows a similar trend of LA conversion as a function of reaction time (Fig. S6). Over 90% of the catalyst mass was recovered after three operating cycles. This result demonstrates that the catalyst recovery and recycling can be facilitated by the macroscopic structure of ZnPBIm-g.

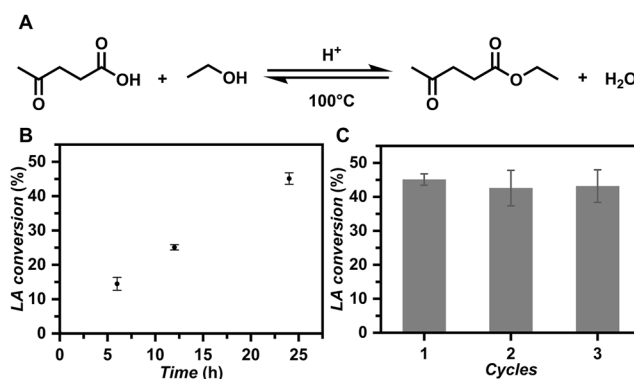


FIG. 2. (a) Reaction scheme of LA esterification with ethanol in the presence of Brønsted acid catalysts. (b) LA conversion (%) over ZnPBIm-g as a function of reaction time at 100 $^\circ\text{C}$ and 24 h of reaction. (c) Recycling test for LA esterification over ZnPBIm-g. Each catalytic cycle was carried out at 100 $^\circ\text{C}$ for 24 h.

TABLE I. LA conversion (%) after 24 h of esterification reaction at 100 °C over different forms of ZnPBIm catalysts with a LA:ethanol molar ratio of 1:1 and catalyst loading of 0.15 g.

Sample	LA conversion (%)
Blank	23
ZnPBIm-g	45
ZnPBIm-g-scrap	50
ZnPBIm-g (after hot filtration test) ^a	21
ZnPBIm-g-bear-shaped	46

^aFor the hot filtration test, LA conversion is determined after 24 h of reaction, in which the catalyst was removed after 6 h from the initial stage and the reaction proceeded without the catalyst for another 18 h.

To confirm the heterogeneous nature of the ZnPBIm-g catalyst, we investigated the leaching of benzimidazole and phosphates by performing the liquid-state ¹H and ³¹P nuclear magnetic resonance (NMR) spectroscopy on the reaction mixture taken after 24 h of esterification. The ¹H NMR spectrum of the reaction mixture obtained from the ZnPBIm-g catalyst [Fig. S7(a)] did not exhibit any peak attributed to the benzimidazole. This observation indicates that there is no leaching of benzimidazole from the catalyst during the esterification. The ³¹P NMR spectrum [Fig. S7(b)] showed a negligible peak at 0 ppm attributed to phosphates. This suggests that phosphate species are also not leached during the reaction.

We performed a hot filtration test under the reaction condition. In a typical procedure, the catalyst was removed after 6 h of reaction and, then, the reaction continued in the absence of the catalyst for another 18 h. After the catalyst removal, a LA conversion of 21% was observed. This value is comparable to that of the blank experiment in the absence of the catalyst (23%) (Table I). The result indicates that ZnPBIm-g monolith acts as a heterogeneous catalyst and the leaching of phosphates is negligible as confirmed by ³¹P NMR. As confirmed by the ICP experiment, the molar ratio of Zn:P of fresh ZnPBIm-g and ZnPBIm-g after the reaction is identical (Table SII).

The appearance of ZnPBIm-g changed from transparent [Fig. S5(a)] to white monolith after 24 h of esterification reaction [Fig. S5(b)]. ZnPBIm-g crystallizes during LA esterification as evidenced by the PXRD [Fig. 1(b-iv)]. SEM images reveal the change of the surface morphology of ZnPBIm-g. The smooth surface of fresh ZnPBIm-g [Fig. 1(d)] changed to polycrystalline grains after LA esterification for 24 h [Fig. 3(a)]. The cross-sectional SEM image of ZnPBIm-g after LA esterification for 24 h displays the interface between the crystalline and glass domains with a distinct crystalline layer of ~7–10 μm [Fig. 3(b)]. The result suggests that the crystallization is induced and propagated from the surface of ZnPBIm-g during the esterification. We did not observe the segregation of the crystallized domain from the glass, and the glass domain serves as a substrate.

We investigated the crystallization of ZnPBIm-g during LA esterification at 100 °C. ZnPBIm-g does not crystallize upon only heating as we observe in DSC [Fig. 1(c)]. Various compounds are present in the reaction mixture of LA esterification, for example, toluene as a solvent and LA and ethanol as reactants. We performed additional experiments by subjecting ZnPBIm-g into different reaction compounds at 100 °C for 24 h and observed the crystallization

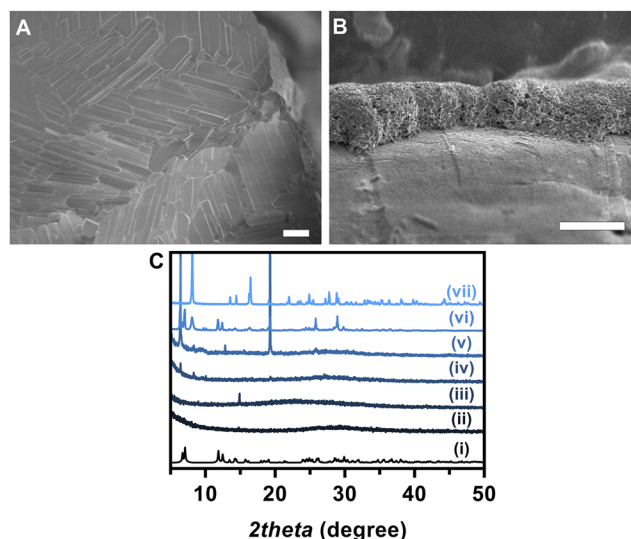


FIG. 3. (a) SEM image and (b) cross-sectional SEM image of ZnPBIm-g after LA esterification for 24 h (the scale bars are 10 μm). (c) PXRD patterns of (i) the simulated pattern of ZnPBIm, (ii) ZnPBIm-g immersed in toluene, (iii) ZnPBIm-g immersed in LA, (iv) ZnPBIm-g immersed in ethanol, (v) ZnPBIm-g immersed in 2 vol. % water-ethanol, (vi) ZnPBIm-g immersed in 2 vol. % water-toluene, and (vii) ZnPBIm-g immersed in water. All solvent immersion was performed at 100 °C for 24 h.

by the PXRD analyses. The immersion of ZnPBIm-g in toluene, LA, or ethanol under heating at 100 °C does not induce crystallization, as confirmed by the PXRD [Figs. 3(c-ii)–3(c-iv)].

Considering that water could form during the esterification reaction as a by-product, ZnPBIm-g was subjected to water immersion under heating at 100 °C for 24 h. Water induces the crystallization of ZnPBIm-g to an unknown crystalline phase [Fig. 3(c-vii)]. By using a mixture of water-toluene or water-ethanol with a water content of 2% by volume, we observed the crystallization of ZnPBIm-g to crystalline ZnPBIm [Figs. 3(c-v) and 3(c-vi)]. The above-mentioned results suggest that a suitable amount of water is required for the formation of crystalline phase of ZnPBIm. The coordination of water to Zn²⁺ in crystallized ZnPBIm-g is confirmed by the PXRD pattern [Fig. 1(b-iv)], which matches with the as-synthesized ZnPBIm showing the hydrated phase [Fig. 1(b-ii)].

The macroscopic structure of ZnPBIm-g monolith facilitates the catalyst recovery as demonstrated in the case of ZnPBIm-g-bear-shaped (Fig. S9) with less than 2% of catalyst mass loss after esterification for 24 h (Table SIII). The sample retains its macroscopic shape after esterification (Fig. S9). As the surface of ZnPBIm-g monoliths crystallizes during LA esterification, the mass loss of the catalyst after the reaction is likely due to the partial detachment of the crystallized domain. The detached crystalline powder is not dissolved nor decomposed in the reaction mixture. We, therefore, did not detect the catalyst loss from the liquid-state NMR spectra taken from the reaction mixture (Fig. S7).

The catalytic activity of ZnPBIm-g in LA esterification is influenced by its external surface area, which is the area defining the external boundary of ZnPBIm-g particles due to the non-porous

nature. We prepared ZnPBIm-g-scrap by crushing ZnPBIm-g into small pieces. As presented in Table I, ZnPBIm-g-scrap shows an enhanced LA conversion with respect to ZnPBIm-g having a similar weight. The external surface area is calculated based on the dimensions and shape of the monolith. In the case of ZnPBIm-g-pellet samples with different external surface areas (e.g., 91, 129, 181, and 257 mm²), LA conversion enhanced with increasing external surface area (Fig. S10). When increasing the external surface area of pellet from 181 to 257 mm², LA conversion did not significantly enhance. This result suggests that further increasing the external surface area of a single catalyst pellet does not contribute to the enhancement of the catalytic activity in LA esterification. In all cases of ZnPBIm-g presented in this study, over 90% of catalyst mass recovery is achieved (Table SIII).

IV. CONCLUSION

We present the macroscopic shaping of ZnPBIm coordination polymer with different shapes and sizes as monolithic heterogeneous catalysts via the crystal–glass phase transformation to achieve an efficient catalyst recovery. Because of the high Brønsted acidity in the structure, the glassy ZnPBIm-g monoliths can catalyze the esterification of LA with ethanol to produce EL. The experimental results confirm the heterogeneous nature of the catalyst during the chemical reaction. Given the macroscopic form and shapable feature of ZnPBIm, facile catalyst recovery can be achieved with over 90% of the catalyst mass recovered. ZnPBIm-g crystallizes during the esterification reaction due to the presence of water as a by-product in the reaction. Crystallization is induced and propagated at the surface of monoliths, while glass domain serves as the substrate. In this manner, the macroscopic shape is retained. The recycling test shows that ZnPBIm-g retains its catalytic activity for at least three consecutive cycles even after surface crystallization.

SUPPLEMENTARY MATERIAL

See the [supplementary material](#) for additional information.

ACKNOWLEDGMENTS

This work was supported by the Japan Society of the Promotion of Science (JSPS) for a Grant-in-Aid for Scientific Research (B) (Grant No. JP21H01950), Challenging Research (Exploratory) (Grant No. JP22K19064), and Transformative Research Areas (A) “Supra-ceramics” (Grant No. JP22H05147) from the Ministry of Education, Culture, Sports, Science and Technology, Japan. This work has also received funding support from the NSRF via the Program Management Unit for Human Resources & Institutional Development, Research and Innovation, Thailand (Grant No. B40G660034).

AUTHOR DECLARATIONS

Conflict of Interest

The authors have no conflicts to declare.

Author Contributions

Thanakorn Tiyyarakul: Conceptualization (equal); Formal analysis (equal); Methodology (equal); Writing – original draft (equal). **Thidarat Imyen:** Conceptualization (equal); Methodology (equal); Validation (equal); Writing – review & editing (equal). **Kanokwan Kongpatpanich:** Funding acquisition (equal); Resources (equal); Supervision (equal). **Teerat Watcharatpong:** Formal analysis (equal); Methodology (equal). **Satoshi Horike:** Conceptualization (equal); Funding acquisition (equal); Resources (equal); Supervision (equal); Writing – review & editing (equal).

DATA AVAILABILITY

The data that support the findings of this study are available from the corresponding authors upon reasonable request.

REFERENCES

- 1 J. Hou, A. F. Sapnik, and T. D. Bennett, *Chem. Sci.* **11**, 310 (2020).
- 2 Y. Chen, X. Huang, S. Zhang, S. Li, S. Cao, X. Pei, J. Zhou, X. Feng, and B. Wang, *J. Am. Chem. Soc.* **138**, 10810 (2016).
- 3 X. Wu, W. Wei, J. Jiang, J. Caro, and A. Huang, *Angew. Chem., Int. Ed.* **57**, 15354 (2018).
- 4 Y. Lu, H. Zhang, J. Y. Chan, R. Ou, H. Zhu, M. Forsyth, E. M. Marijanovic, C. M. Doherty, P. J. Marriott, M. M. B. Holl, and H. Wang, *Angew. Chem., Int. Ed.* **58**, 16928 (2019).
- 5 M. Wickenheisser, A. Herbst, R. Tannert, B. Milow, and C. Janiak, *Microporous Mesoporous Mater.* **215**, 143 (2015).
- 6 M. Liu, R. D. McGillicuddy, H. Vuong, S. Tao, A. H. Slavney, M. I. Gonzalez, S. J. L. Billinge, and J. A. Mason, *J. Am. Chem. Soc.* **143**, 2801 (2021).
- 7 D. Umeyama, S. Horike, M. Inukai, and S. Kitagawa, *J. Am. Chem. Soc.* **135**, 11345 (2013).
- 8 R. Banerjee, A. Phan, B. Wang, C. Knobler, H. Furukawa, M. O’Keeffe, and O. M. Yaghi, *Science* **319**, 939 (2008).
- 9 A. Qiao, T. D. Bennett, H. Tao, A. Krajnc, G. Mali, C. M. Doherty, A. W. Thornton, J. C. Mauro, G. N. Greaves, and Y. Yue, *Sci. Adv.* **4**, ea06827 (2018).
- 10 R. Gaillac, P. Pullumbi, K. A. Beyer, K. W. Chapman, D. A. Keen, T. D. Bennett, and F.-X. Coudert, *Nat. Mater.* **16**, 1149 (2017).
- 11 T. Watcharatpong, T. Pila, T. Maihom, T. Ogawa, T. Kurihara, K. Ohara, T. Inoue, H. Tabé, Y.-S. Wei, K. Kongpatpanich, and S. Horike, *Chem. Sci.* **13**, 11422 (2022).
- 12 K. S. Park, Z. Ni, A. P. Côté, J. Y. Choi, R. Huang, F. J. Uribe-Romo, H. K. Chae, M. O’Keeffe, and O. M. Yaghi, *Proc. Natl. Acad. Sci. U. S. A.* **103**, 10186 (2006).
- 13 Y. Hirai, T. Nakanishi, Y. Kitagawa, K. Fushimi, T. Seki, H. Ito, H. Fueno, K. Tanaka, T. Satoh, and Y. Hasegawa, *Inorg. Chem.* **54**, 4364 (2015).
- 14 K. Tanaka, Y. Tago, M. Kondo, Y. Watanabe, K. Nishio, T. Hitosugi, and M. Moriya, *Nano Lett.* **20**, 8200 (2020).
- 15 N. Ma, S. Kosasang, A. Yoshida, and S. Horike, *Chem. Sci.* **12**, 5818 (2021).
- 16 C. Thanaphatkosol, N. Ma, K. Kageyama, T. Watcharatpong, T. Tiyyarakul, K. Kongpatpanich, and S. Horike, *Chem. Commun.* **58**, 6064 (2022).
- 17 P. Dughuntod, T. Imyen, W. Wannapakdee, T. Yutthalekha, S. Salakhum, and C. Wattanakit, *RSC Adv.* **9**, 18087 (2019).
- 18 T. D. Bennett, Y. Yue, P. Li, A. Qiao, H. Tao, N. G. Greaves, T. Richards, G. I. Lampronti, S. A. T. Redfern, F. Blanc, O. K. Farha, J. T. Hupp, A. K. Cheetham, and D. A. Keen, *J. Am. Chem. Soc.* **138**, 3484 (2016).
- 19 F. G. Cirujano, A. Corma, and F. X. Llabrés i Xamena, *Chem. Eng. Sci.* **124**, 52 (2015).